ELSEVIER

PII: S0301-5629(02)00652-X

● *Original Contribution*

THE EFFECTS OF DIGITIZATION ON THE ELASTOGRAPHIC SIGNAL-TO-NOISE RATIO

S. Srinivasan,*[†] F. Kallel*[†] and J. Ophir*[†]

*Department of Radiology, Ultrasonics Laboratory, The University of Texas Medical School, Houston, TX, USA;
and [†]Electrical and Computer Engineering Department, University of Houston, Houston, TX, USA

Abstract—In elastography, the tissue under investigation is compressed and the resulting strain is estimated from the gradient of the displacement (time-delay) estimates. The displacements are typically estimated by cross-correlating the radiofrequency (RF) ultrasound signals of the pre- and postcompressed tissue. One of the parameters used to quantify the resulting quality of the elastogram is the elastographic signal-to-noise ratio (SNR_e). For a uniformly elastic target (a single elastic modulus), the dependence of the SNR_e on the applied strain has a bandpass characteristic that has been termed the strain filter. Theoretical expressions for the upper bound on the strain filter were developed earlier. Yet, simulated as well as experimental strain filters derived from uniformly elastic phantoms deviate from these upper bounds. The failure to achieve the upper bounds could be partially attributed to the fact that, in both simulations and experiments, the RF signals used to compute the TDEs are sampled and quantized. Using simulated models of uniformly elastic phantoms, a study of the dependence of the strain filter on the quantization and sampling rates was performed. The results indicated that the strain filter improves with both the sampling rate and the quantization, as expected. A theoretical analysis was done to incorporate quantization as a derating factor to the strain filter. (E-mail: Jonathan.Ophir@uth.tmc.edu)   © 2002 World Federation for Ultrasound in Medicine & Biology.

Key Words: Ultrasound, Elastography, Correlation coefficient, SNR, Sampling, Quantization, Digitization.

INTRODUCTION

Ultrasonic techniques for measuring the elastic properties of compliant tissue generally rely on the estimation of strain, stress and Young's and shear moduli of the tissue. Elastography, a technique of estimating strain using differential displacements of the tissue elements, has been well established (Ophir et al. 1991, 1996, 1997, 1999). Strain estimation techniques can be classified into either coherent or incoherent techniques. Coherent techniques are based on time-domain cross-correlation (Ophir et al. 1991; Céspedes 1993) or on Fourier-based speckle phase-tracking (O'Donnell et al. 1991) time-delay estimation (TDEs), while incoherent estimators include spectral cross-correlation (Varghese et al. 2000) and optical-flow–based techniques (Bertrand et al. 1989). The commonly used time-domain cross-correlation techniques measure the time delay (the strain is estimated as the gradient of the time-delay) between the

pre- and the postcompression A-lines. These A-lines are often modeled as a convolution between the system impulse response (the point-spread function) and the tissue scatterers. Stretching the postcompression A-lines is typically done to undo the effects of the mechanical compression on the signal (Céspedes and Ophir 1993; Varghese and Ophir 1997a). However, a perfect match between the pre- and postcompression A-lines is not achievable. This is because the transmitted impulse response gets stretched simultaneously when the stretching compensates for the tissue motion and, also, because of the lateral and elevational motion of the scatterers. The decorrelation between the pre- and postcompression A-lines increases with the applied strain (Varghese and Ophir 1997a) and corrupts the strain estimates at large strains (typically > 10%). On the other hand, for very low strains (typically < 0.1%), the amplitude of the measurement noise (determined by the sonographic signal-to-noise ratio, (SNR_s) relative to the measured strain is typically high. Hence, there is an intermediate range of strains for which high elastographic signal-to-noise ratio (SNR_e), defined as the ratio of the mean value (μ_m) of the

measured strain to the standard deviation (SD) of the measured strain (σ_m), can be obtained. A plot of SNR_e as a function of the applied strain looks similar to a bandpass filter (in the strain domain) and has been termed the strain filter (SF) (Varghese and Ophir 1997b).

The SF is sensitive to several parameters that can be categorized as the acoustic parameters (such as the SNR_s, the transducer center frequency and bandwidth), the algorithmic parameters (such as the window size and the window overlap), and the mechanical parameters (such as the applied strain and the strain distribution). A functional relationship between SNR_e and strain has been established by Varghese and Ophir (1997b) for boxcar-shaped bandpass ultrasonic RF signal and noise spectra. Details on the SF are provided in Appendix A. Such a SF assumes ideal conditions like stationary ultrasonic and noise signals, no attenuation and pure axial time delays. However, in practice, several derating factors, such as frequency-dependent attenuation, lateral and elevational tissue motion, are present. Previous work by Varghese and Ophir (1997c) and Kallel et al. (1997) has accounted for the effects of frequency-dependent attenuation and lateral motion on the SF, respectively. In addition to these derating factors, it is expected that the digitization parameters (sampling frequency and the amplitude quantization) affect the strain-filter as well. These effects are important because all modern data-acquisition systems deal with digitized signals and, hence, the choice of sampling frequency and quantization is critical to the understanding of the ultimate performance limitations imposed on the elastographic system.

This paper is organized as follows. A brief introduction to the utility of the SF as a benchmark for measuring SNR_e is provided in the next section and the subsequent sections detail the digitization issues that may result in corruption of the SF under certain conditions.

The strain filter

The SF is the functional dependence of the SNR_e (defined as the ratio of the mean value, μ_m, of the exstimated strain to the SD of the measured starin, σ_m, for different values of the applied strain) with the applied strains. The expression for the upper bound of the SNR$_e$ is given by

$$SNR_e = \frac{S}{\sigma_s}, \qquad (1)$$

where $_s$ is the applied strain and σ_s is the lower bound of the SD of the measured strain, given in Céspedes et al. (1995b) as

$$\sigma_s^2 = \frac{2\sigma_{ZZLB}^2}{T\Delta T}, \qquad (2)$$

where T is the segment length used in TDEs, ΔT is the separation between adjacent time segments (used to compute the strain), and σ_{ZZLB}^2 is the Ziv–Zakai lower bound on the variance (Appendix A). The bound on σ_{ZZLB}^2 is derived in Weinstein and Weiss (1984a, 1984b). The combined SNR (SNR_c) used in obtaining σ_{ZZLB} is derived (Varghese and Ophir 1997b) as

$$SNR_c = \frac{SNR_\rho SNR_s}{1 + SNR_\rho + SNR_s}. \qquad (3)$$

Here, SNR_ρ is the correlation SNR (Céspedes and Ophir 1993), given by

$$SNR_\rho = \frac{\rho}{1 - \rho}, \qquad (4)$$

where ρ is the correlation coefficient (defined as the amplitude of the cross-correlation peak normalized by the autocorrelation amplitudes at zero lag). The upper bound on the SNR_e as a function of strain has a bandpass characteristic, as shown in Fig. 1a. Here, two regions of the Ziv–Zakai lower bound, namely the Cramér–Rao lower bound (CRLB) and the Barankin bound (BB), are shown. The CRLB corresponds to the region where there are no ambiguities in the identification of the correct cross-correlation peak (*i.e.,* there is ambiguity only in the phase measurement at the peak), and the BB corresponds to the region where there are ambiguities in the identification of the correct cross-correlation peak (*i.e.,* there are ambiguities in both the location of the peak and the phase measurement at the peak). Details on these bounds can be found in Weinstein and Weiss (1984a). The variance of the TDEs in the CRLB is given (Walker and Trahey 1995; Céspedes et al. 1997) by

$$\sigma_{CRLB}^2 \cong \frac{3}{\pi^2 T f_o^3 (B^3 + 12B)} \left(\left(1 + \frac{1}{SNR_c}\right)^2 - 1 \right), \qquad (5)$$

where f_o is the center frequency, and B is the fractional band width. Combining eqns (1), (2), (3), (4) and (5), the expression for SNR_e in the CRLB becomes

$$SNR_e \cong \frac{\pi s T \sqrt{\Delta T(f_o^3(B^3 + 12B)}}{\sqrt{6\left(\left(1 + \frac{1}{SNR_c}\right)^2 - 1\right)}}. \qquad (6)$$

Although eqn (6) suggests a linear increase of the SNR_e with strain in the CRLB, the SNR_e increases at a less than linear rate for strains > 1%. This is due to the dependence of SNR_c (and SNR_ρ) on the applied strain (Fig. 1b). SNR_ρ decreases with increasing strain due to decorrela-
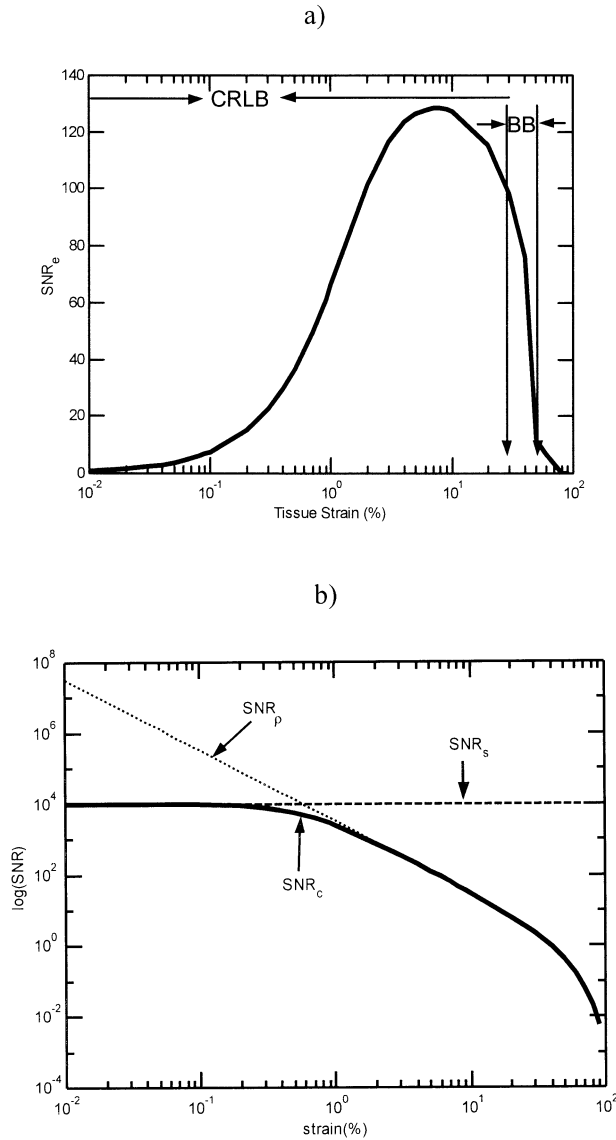
a)

b)

Fig. 1. (a) The SF illustrating the distinct regions of strain estimation obtained using the expressions for σ_{ZZLB} and (b) SNR_s, SNR_ρ and SNR_c plotted as functions of strain. The SF was obtained for a 5-MHz, 50% fractional bandwidth transducer using an observation window of 3 mm and a window overlap of 50% at an SNR_s of 30 dB. The CRLB refers to the Cramér–Rao lower bound that is dominated by random noise. The *BB* refers to the Barankin bound that is dominated by decorrelation noise.

tion, as explained previously. The variation of ρ with strain was established in Varghese and Ophir (1997b) and is given in Appendix C, (eqn (C15)). When SNR_ρ is larger than SNR_s (strains less than 0.3%), the SNR_c asymptotes toward SNR_s for decreasing strains. In this region, the SNR_e shows an asymptotic decrease with decreasing strain (Fig. 1a). When SNR_ρ is comparable to SNR_s (strains between 0.3% and 1%), SNR_e increases linearly with the strain. An inflexion point occurs at

around 1% strain (Fig. 1b) and the SNR_e starts deviating from a linear increase beyond this strain value. For SNR_ρ that is significantly lower than SNR_s, the SF drops due to a large increase in the variance. This happens when the product $B.T.SNR_c$ exceeds a threshold (*i.e.,* the Barankin bound is reached). For very high strains ($> 20\%$), another threshold region is entered and the SNR drops further (due to ambiguity in both the amplitude and phase measurements of the cross-correlation peak).

The width of the strain-filter at a given SNR_e, defined as the elastographic dynamic range (DR_e), is an indicator of the range of strains over which reliable strain estimates can be made. The height of the strain filter, the SNR_e, is a direct indicator of the quality of the strain estimate. The area under the SF may also be used as a gross numerical indicator of overall quality of the elastogram.

Simulated and experimental SFs deviate from the theoretical SF due to several factors, such as deviation from a rectangular spectrum, violation of the stationarity assumptions (frequency- and depth-dependent attenuation, lateral and elevational tissue motion, *etc.*) and digitization effects. The attenuation and the lateral motion have previously been accounted for as nonstationary derating factors in the SF (Varghese and Ophir 1997c; Kallel et al. 1997). In the next section, we investigate the effects of digitization.

Digitization

An appropriate digitization of the RF A-lines is necessary for a high SNR_e. In the sections below, we investigate the effects of sampling and quantization on the strain filter.

In the absence of noise and amplitude quantization, sampling at or above the Nyquist rate is sufficient to reproduce the analog signal and, hence, to obtain perfect TDEs. However, quantization and noise corrupt the signal, thereby affecting the TDEs. It is to be noted that, for cross-correlation–based algorithms, interpolation of the cross-correlation function introduces errors that vary according to the sampling rate, unless the shape of the cross-correlation function is known. TDEs in elastography utilizes linear stretching, whose accuracy improves with a decrease in the sampling interval (Céspedes et al. 1995a). Additionally, the bias and the variance of the TDEs are inversely proportional to the sampling rate when interpolation techniques (such as parabolic or cosine) are used on the cross-correlation function, thereby improving the performance with sampling rate (Céspedes et al. 1995a). It has been demonstrated that these interpolation techniques perform poorly if the all-positive-samples condition, around the peak of the cross-correlation function, is violated (Céspedes 1993). This condition is violated if the sampling frequency (f_s) is less

than 6 times the maximum frequency of interest in the signal (f_1) i.e., $f_s < 6f_1$. For f_s exceeding this value, marginal improvement with oversampling is expected. It is to be noted that sampling is not a fundamental limitation of elastographic systems (unlike the derating factors, such as lateral/elevational motion or attenuation), and can be improved by incorporating good interpolation techniques or by oversampling.

The quantization noise depends on the type of the signal and cannot usually be modeled as additive noise. For uniform quantization, the noise is higher where the amplitude of the signal is small and lower where the amplitude is large. Hence, the role of quantization in TDEs is important. In elastography, quantization results in corruption of the relative amplitude and phase information and especially affects the estimation of low strains, as is explained as follows. For low strains, the delays between the A-lines are smaller than the sample intervals and, hence, the amplitude differences between the pre- and postcompression A-lines reflect the time delay between them. Small differences in signal amplitudes are most likely to be eliminated by quantizing the signals resulting in inaccurate TDEs and strain for such quantized signals.

METHODS

One-dimensional simulations in MATLAB (Mathworks, Inc., Natick, MA) were used to generate pre- and postcompression RF signals, corresponding to a 30-mm target segment, and were sampled at several sampling frequencies from 24 MHz to 192 MHz. In addition to 1-D simulations, 2-D simulations were used on a $40 \times 40 \text{ mm}^2$ uniformly elastic target to show the dependence of the SF on sampling. However, 1-D simulations were preferred over 2-D simulations for two reasons: a) lateral motion and beam effects have been accounted for as derating factors in the SF, and b) significantly smaller simulation time is required when statistical analysis over several parameters, such as the window size, overlap, center frequency, bandwidth, SNR_s, sampling frequency and quantization, is performed.

The speed of sound in tissue was assumed to be constant at 1540 m/s. The 1-D point spread function (PSF), which is the impulse response of the system, was simulated using a Gaussian-modulated cosine pulse with a 5-MHz center frequency and a 50% half-power relative bandwidth. The scattering function was modeled as a normal distribution of scatterer amplitudes (Meunier and Bertrand 1995a, 1995b; Walker and Trahey 1995). The PSF was convolved with the scattering function to obtain the RF signal. The postcompression signals were generated after applying a uniform compression of the point scatterers (Céspedes 1993) and convolving the com-

pressed point scatterers with the original PSF. The SNR_s was varied from 20 to 40 dB by adding other uncorrelated RF A-lines to both the pre- and postcompression A-lines. We used these other RF A-lines as noise sources (having the same power spectral shape as the signal A-lines) to model noise in the tissue. Such noise could arise from unwanted tissue motion, such as vibration, relaxation and other viscous effects. For example, phase aberration has been shown to be a significant source of decorrelation in both elastography and sonography (Varghese et al. 2001; Trahey and Smith 1988). The spectra of the ultrasonic noise resemble the shape of the signal spectrum because the receiver has a bandpass Gaussian transfer function. Noise sources beyond the receiver could have wideband spectra and are not considered here. The resulting postcompression RF A-line was then stretched by an amount equal and opposite to the applied strain.

For the 2-D simulations, 2-D displacement and echo-generation models were used to generate displacement and RF A-lines of a uniformly elastic phantom. The medium was simulated as a set of uniformly distributed scatterers (with a density of 40 scatterers/pulse-width). The 2-D PSF was simulated using a Gaussian-modulated cosine pulse with a 5-MHz center frequency, and a 50% fractional bandwidth and a 1-mm full-width half-maximum (FWHM) Gaussian beamwidth (Kallel et al. 1997). The pre- and postcompression RF A-lines were obtained by convolving the PSF with the scattering distribution before and after compression.

The A-lines were segmented into windows of lengths varying from 1 to 3 mm, with several overlaps varying from 0% to 80%. The cross-correlation function for these segments was computed as:

$$R_{xy}(\tau) = IFT\{X(w_k)Y^*(w_k)\}, \tag{7}$$

where $X(w_k)$ and $Y(w_k)$ are the discrete-time Fourier transforms of the pre- and postcompression A-line segments, $Y^*(w_k)$ is the complex conjugate of $Y(w_k)$, and IFT is the inverse Fourier transform.

The value of ρ was computed and used in the SF equations to calculate the simulated SF. Specifically, the measured value of ρ was used in eqns (1) through (5) to compute the SNR_e (and, hence, the SF). The reason for using such an estimate, instead of measuring the SNR_e directly from the elastogram, is explained in Srinivasan et al. (2002) and, for convenience, is also briefly explained in Appendix B. The study was conducted for several sampling frequencies (f_s), window length (T), window separation (ΔT), center frequency (f_o), band width (B), and SNR_s. Additional studies with respect to variation in the PSF, the scatter function, noise model,

band-limitation of the PSF, downsampling and stretch factor were performed, and are discussed later.

RESULTS

Sampling frequency

A simulation study with values of f_s ranging from 24 MHz to 192 MHz was performed, and the results are summarized below. Typical SFs for sampling frequencies of 24 MHz, 48 MHz, 96 MHz and 192 MHz at a SNR_s of 40 dB using 3-mm windows with 50% overlap are shown in Fig. 2a. The SFs tend to asymptote to the theoretical SF with increasing sampling frequency for strains < 10%. For higher strains (> 10%), the decorrelation effects preclude the observation of such behavior. It is to be noted that the SFs have a wider dynamic range than those reported in Varghese and Ophir (1997b), due to the use of a different bandwidth definition. We use a half-power bandwidth, but a half-amplitude bandwidth was used in the previous work. Assuming Gaussian distributions of the simulated SNR_e values (at each strain), a statistical analysis was performed to show that the mean values of the simulated SFs at several sampling frequencies differed from each other significantly (p values < 0.01) for f_s values of 24 MHz, 48 MHz and 96 MHz for strain values less than 6%. No statistically significant difference was found between the SFs at f_s values of 96 MHz and 192 MHz over 50 independent realizations. For higher strains (> 6%), no statistically significant difference was found (p values > 0.01) between the simulated SFs. Figure 2b shows the correlation coefficients that correspond to the SFs in Fig. 2a. The SDs in ρ (σ_ρ) are less than 0.004ρ. A statistical analysis was performed to show that the mean values of the correlation coefficients at several sampling frequencies differed from each other significantly (p-values < 0.01) at strains less than 6%.

SNR_e is sensitive to change in ρ, due to the nonlinear relationship with ρ, as evident from eqns (1) through (5). Small changes in ρ result in large changes in SNR_e that motivates the need for accurate stretching, and also the use of adaptive stretching techniques like those suggested in Alam et al. (1998) and Chaturvedi et al. (1998) for nonhomogenous materials. For example, the change in SNR_e due to using $(\rho - \sigma_\rho)$ as opposed to using ρ (*i.e.*, $SNR_e|_\rho - SNR_e|_{\rho - \sigma_\rho}$) is larger (Fig. 3) than the SDs in SNR_e (Fig. 2a). We attribute such high SDs to the nonlinear relationship between SNR_e and ρ that enhances small variations in ρ. A sensitivity analysis of SNR_e with respect to change in ρ was performed (Appendix C), and the results indicate that such a behavior is expected.

SNR_e is an indicator of the quality of the SF (and the elastogram), and the dynamic range (the range of strains for which the SNR_e exceeds a threshold) is an indicator of the amount of reliable information contained in the SF. The area contained under the SF would, therefore, be an
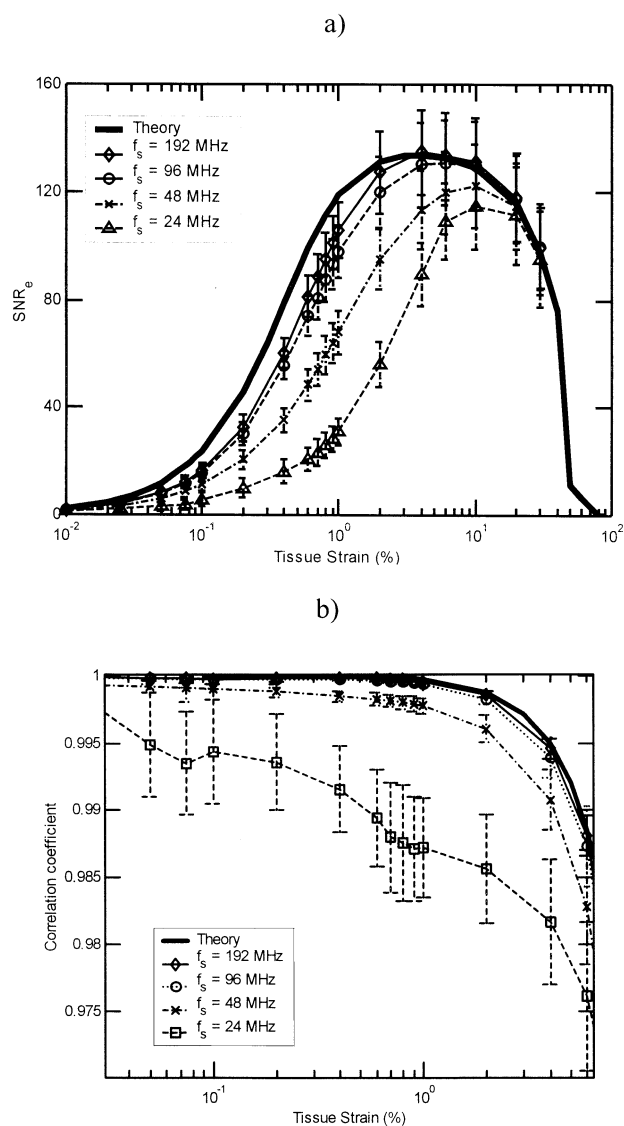

Fig. 2. (a) Simulated SFs and (b) the correlation coefficient as a function of strain for various sampling frequencies (f_s) for a 5-MHz, 50% fractional band width Gaussian PSF, and 3-mm window with a 50% overlap on a uniformly elastic phantom at an SNR_s of 40 dB. The error bars correspond to $\pm$ σ over 50 independent realizations.

indicator of both the quality and the quantity of information contained. Such an area measure incorporates both the SNR_e and the dynamic range and could be useful in quantifying the SF, thereby facilitating a relatively simple comparison of strain-estimation techniques. Henceforth, this SF area is called the "figure-of-merit" (FOM). The FOM normalized by the theoretical SF area (corresponding to strains ranging from 0.1% to 30%) as a function of the normalized sampling rate (f_s/f_o) is shown in Fig. 4. The areas were computed as the sum of the trapezoidal areas between adjacent strain estimates in
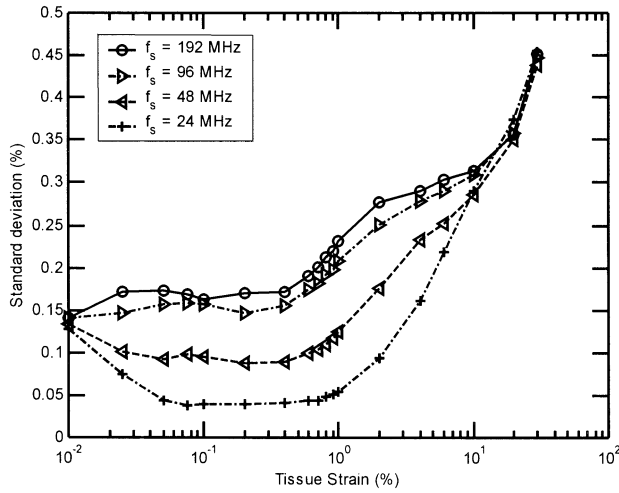
Fig. 3. SD in SNR_e using the SDs in ρ of the simulated SFs for various sampling frequencies (f_s) for a 5-MHz, 50% fractional bandwidth Gaussian PSF, and 3-mm window with a 50% overlap on a uniformly elastic phantom at an SNR_s of 40 dB.

the SF. It can be seen that the mean statistics show a clear trend. The error bars represent $\pm \sigma$. A total of 50 independent realizations were used to compute these statistics. The difference in the means at a normalized sampling rate of 5 and a normalized sampling rate of 10 were statistically significant (p-values $<$ 0.01).

The 2-D simulation results are summarized in Figs. 5 and 6. Figure 5a shows the theoretical (Kallel et al. 1997) and the simulated SFs at the axis of lateral symmetry (20 mm from either edge) for the simulations on a 40 $\times$ 40
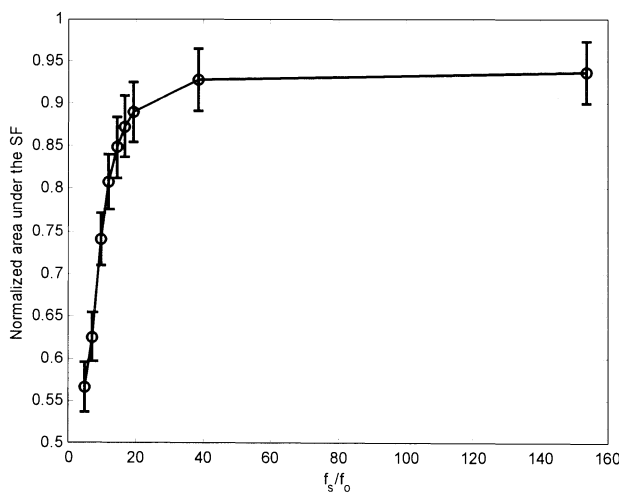

Fig. 4. Asymptotic improvement of the figure-of-merit with f_s for a 5-MHz, 50% fractional bandwidth Gaussian PSF, and 3-mm window with a 50% overlap at an SNR_s of 40 dB. The error bars correspond to $\pm \sigma$ over 50 independent realizations.
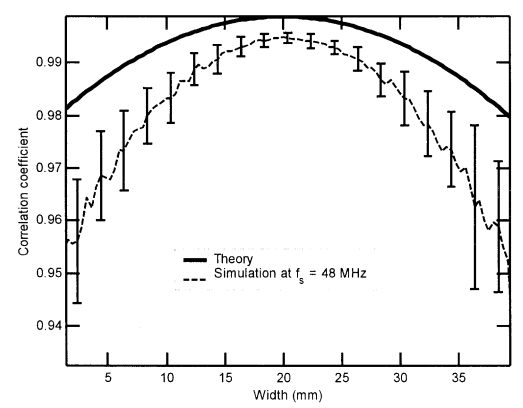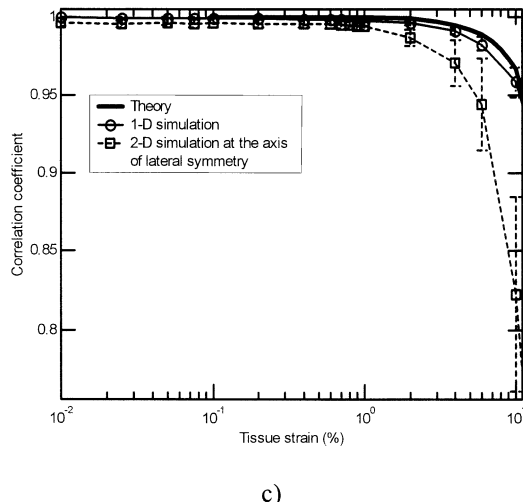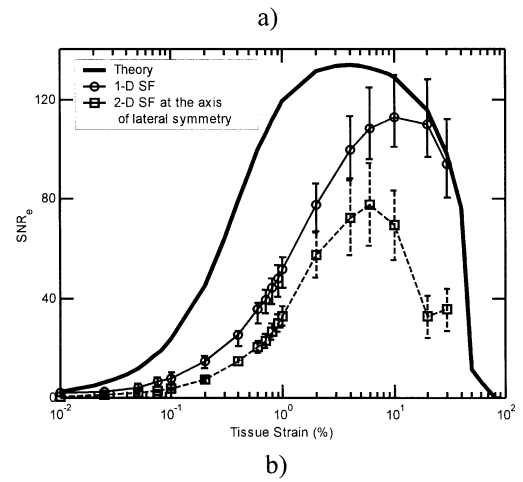

Fig. 5. (a) 2-D SF at the axis of lateral symmetry and comparison with the theoretical and 1-D SFs; (b) the correlation coefficient as a function of strain at the axis of lateral symmetry; and (c) the correlation coefficients as a function of the lateral location for a strain of 1%. The simulations were performed on a 40 $\times$ 40 mm^2 uniformly elastic phantom with a 5-MHz, 50% fractional bandwidth Gaussian PSF, and 3-mm window with a 50% overlap at an SNR_s of 40 dB and a sampling frequency (f_s) of 48 MHz. The error bars correspond to $\pm \sigma$ over 50 independent realizations.
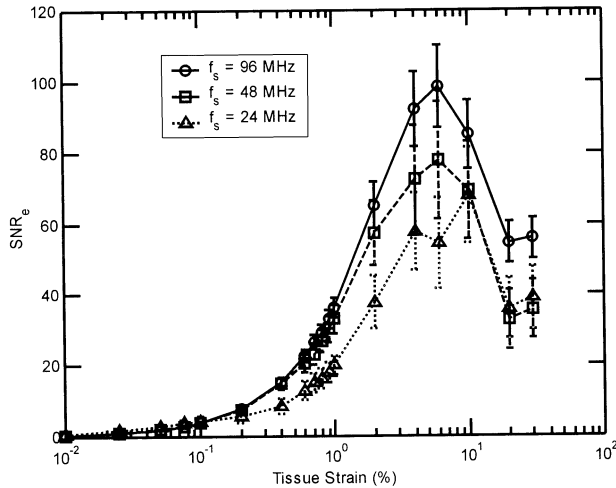
Fig. 6. Simulated SFs for various sampling frequencies (f_s) for a 5-MHz, 50% fractional bandwidth Gaussian PSF, and 3-mm window with a 50% overlap on a 2-D simulation of a uniformly elastic phantom of 40×40 mm² at an SNR_s of 40 dB. The error bars correspond to $\pm \sigma$ over 50 independent realizations.

Fig. 7. SFs for (a) several bit resolutions at an SNR_s of 40 dB; and (b) comparison of the SFs for several bit resolutions at an infinite SNR_s. The SFs were obtained for a 5-MHz, 50% fractional bandwidth Gaussian PSF, and 3-mm window with a 50% overlap on a uniformly elastic phantom sample at a sampling frequency (f_s) of 96 MHz. The error bars correspond to $\pm \sigma$ over 50 independent realizations.

mm² uniformly elastic phantom with a 100-element array transducer (pitch = 0.4 mm) and a Gaussian beam profile of beamwidth (half-amplitude) of 0.7 mm. The SF at the axis of lateral symmetry has smaller values of the SNR_e and dynamic range than those corresponding to the 1-D SF. This is attributed to the nonrigid scatterer motion (in the lateral direction) within the beamwidth. The values of ρ corresponding to the SFs in Fig. 5a are shown as a function of strain in Fig. 5b. Figure 5c shows the correlation coefficient as a function of the lateral location at a strain of 1%. The change in the values of ρ with the lateral location are similar to those obtained by Kallel et al. (1997). A statistical comparison of the SFs over 50 realizations was performed to compare SFs based on a 95% confidence interval (p-value < 0.05). The true means of the simulated SFs were found to be significantly different from one another, as can be seen in Fig. 5a. Figure 6 shows the improvement in the SF with f_s for the 2-D simulations. The difference of the SFs at values of f_s of 96 MHz and 24 MHz was statistically significant (p-value < 0.01).

The 2-D simulations produce SFs that have lower values of SNR_e and dynamic range than the 1-D simulation. This is due to the lateral motion and the presence of a beam in the 2-D simulation. It is to be noted that derating the SFs to accommodate lateral motion (Kallel et al. 1997) still does not account for the nonrigid scatterer motion within the beam. Therefore, the SF at the axis of lateral symmetry (*i.e.,* at 20 mm in Fig. 5a) is generally inferior to that of the 1-D simulation. An analysis of nonuniform displacement within the beam
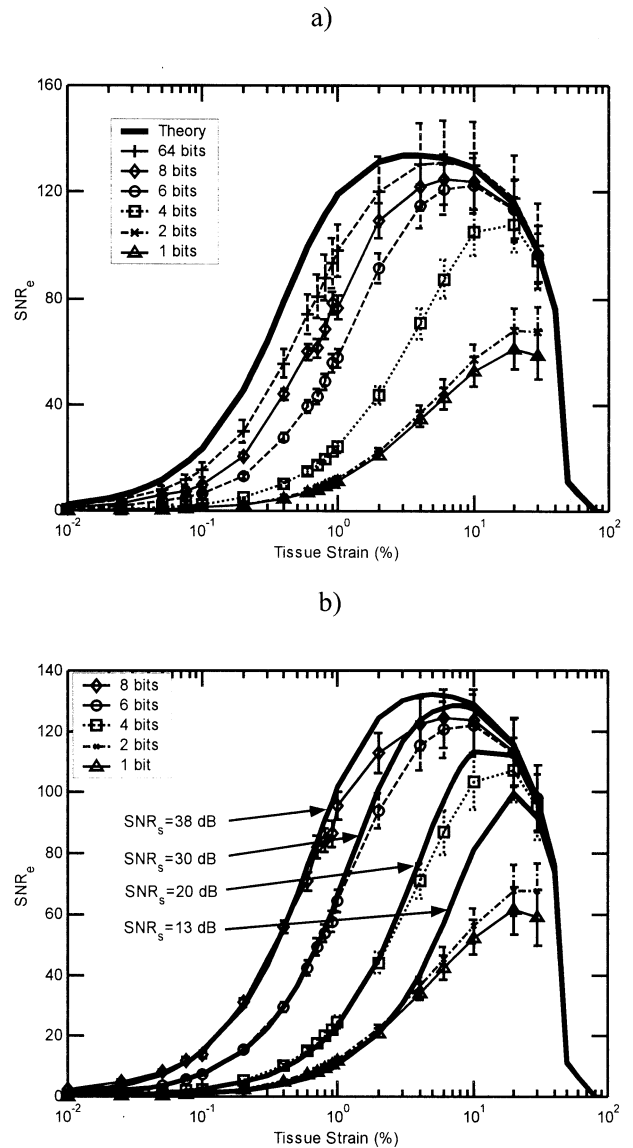
width needs to be done to account for such a difference between the theoretical and simulation results.

Quantization

An empirical relationship between the number of quantization bits and the effective SNR_s of the RF A-lines can be established as follows. For a signal that is quantized, the noise introduced due to quantization can be modeled as an effective SNR (SNR_q) of the signal

(Bendat and Piersol 1986). In elastography, the SF computed using quantized pre- and postcompression RF signals can be considered as analogous to having nonquantized RF signals (*i.e.,* analog values of the signal amplitudes), but with an effectively reduced SNR_s. Thus, an empirical correspondence between SNR_q and SNR_s can be established, thereby incorporating quantization as a derating factor of the SF.

Quantization at several bit resolutions, from 1 to 64 bits, was tried for several values of f_s. The results are summarized as follows. Figure 7a shows the improvement in the SF with the bit resolution. It can be seen that the improvement in performance with the number of bits is asymptotic and no significant differences between an 8-bit and 64-bit quantization can be seen. Values of SNR_e approximately equal to those corresponding to these derated SFs can be obtained empirically by changing the SNR_s. Thus, an empirical correspondence between a bit resolution and a SNR_s can be obtained by comparing SFs, even though quantization noise cannot be modeled as an additive noise, while the SF theory assumes additive uncorrelated noise. Such a correspondence of the bit resolution to an approximate SNR_s is shown in Fig. 7b. Here, the simulations for the quantization rate are done in the absence of additive noise (at an infinite SNR_s). It can be seen that an 8-bit quantization corresponds roughly to an SNR_s of 38 dB, (6-bit $\approx$ 30 dB SNR_s, 4-bit $\approx$ 20 dB SNR_s, and 2-bit $\approx$ 13 dB SNR_s). This correspondence is based on the mean statistics, as explained previously.

The RF A-line is assumed to be a cosine signal with an envelope that is Rayleigh-distributed (Zagzebski et al. 1999). Because the Rayleigh distribution allows infinite signal amplitudes that are not realizable in simulations and experiments, the RF A-line is saturated at some arbitrary amplitude and the effective bit resolution is found for the "chopped" distribution. Such an empirical procedure facilitates a comparison between simulations and the experiments and is detailed below.

An analytical expression for the SNR_s introduced due to quantization (SNR_q) can be obtained as follows. The RF A-line is assumed to be a cosine signal with an envelope that is Rayleigh-distributed. The mean square error (E) due to uniform quantization is given by

$$E = \frac{S^2}{12} , \qquad (8)$$

where S is the height of the quantizing levels (Bendat and

Piersol 1986). For a dynamic range D (peak-to-peak amplitude) of the signal that is quantized into m bits, we obtain

$$E = \frac{D^2}{12} 2^{-2m} . \qquad (9)$$

For a cosine signal of peak amplitude A, we have $D = 2A$. Therefore, for each cycle in the RF A-line, the SNR due to quantization becomes

$$SNR_q = \frac{A^2/2}{E} = \frac{3}{2} 2^{2m} , \qquad (10)$$

where m is the number of bits used for quantization of that cycle. The quantity m varies with the peak amplitude of the cosine signal and is, therefore, Rayleigh-distributed. For an 8-bit quantization, the maximum value of SNR_q would be approximately 50 dB. However, not all the bits get utilized for each cycle of the A-line. This is because the peak amplitude of the cosine signal is Rayleigh-distributed and m varies with the amplitude of the cosine signal. Hence, the SNR_q has to be derated according to an effective number of bits, which is less than the actual number of bits used. An empirical expression for the effective bit resolution is derived as follows. For a zero mean RF A-line, $m-1$ bits are used for positive amplitudes. The Rayleigh probability density function (pdf) of the amplitudes is of the form

$$f(A) = \frac{A}{\sigma^2} e^{\frac{-A^2}{2\sigma^2}} , \qquad (11)$$

where A is the amplitude and σ is the SD of the pdf. Because, in practice, the dynamic range of the amplitudes is limited, we saturate the signals at an arbitrary value of $A = k\sigma$. Quantizing these amplitudes (from 0 to $k\sigma$) uniformly into t ($t = 2^{n-1} - 1$) amplitude levels, where n is the available bit resolution, we assign a set of probabilities for the discrete amplitudes. These probabilities are obtained as the area of the pdf between adjacent amplitude levels ($l - 1$ and l) given by

$$P(l) = \int_{(l-1)\frac{k\sigma}{t}}^{l\frac{k\sigma}{t}} f(A)dA. \qquad (12)$$

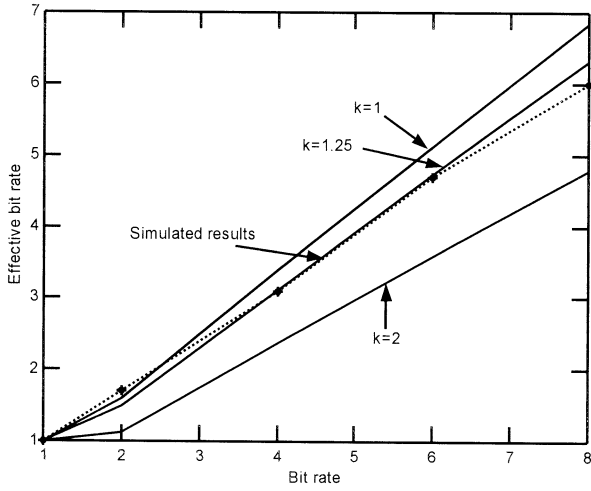The expected number of the amplitude levels is, therefore, given by

Fig. 8. Effective bit resolution plotted a function of the bit resolution for several values of k for both the empirical estimates and the simulations.
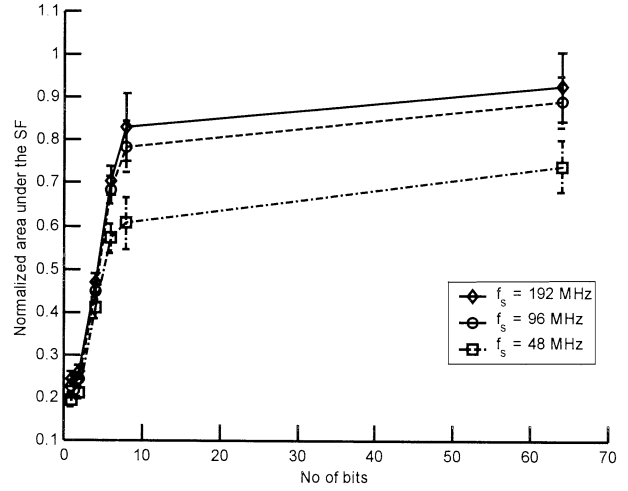

Fig. 9. Asymptotic improvement of the figure-of-merit with the bit rate for a 5-MHz, 50% fractional bandwidth Gaussian PSF and 3-mm window with a 50% overlap at a SNR_s of 40 dB.

$$E(t) = \left(\sum_{l=1}^{l=t} lP(l) + (t+1) \int_{k\sigma}^{\infty} f(A)dA \right)$$

$$= \left(\sum_{l=1}^{l=t} \int_{(l-1)\frac{k\sigma}{t}}^{l\frac{k\sigma}{t}} f(A)dA + (t+1) \int_{k\sigma}^{\infty} f(A)dA \right).$$

$$(13)$$

Because a total of $(t+1)$ amplitude levels correspond to a bit resolution of n, the effective bit resolution (m) is obtained as:

$$m = n\frac{E(t)}{t+1}$$

$$= n\left(\frac{\sum_{l=1}^{l=t} \int_{(l-1)\frac{k\sigma}{t}}^{l\frac{k\sigma}{t}} f(A)dA + (t+1) \int_{k\sigma}^{\infty} f(A)dA}{(t+1)} \right). \quad (14)$$

m depends on k and n. Figure 8 shows m as a function of n for several values of $k\sigma$, obtained using eqn (14). The simulated values of m, shown as the dotted lines in Fig. 8 were obtained using eqn (10) with the values of SNR_s in Fig. 7b substituting the values of SNR_q in eqn (10) (*i.e.,* the values of SNR_q in eqn (10) were replaced by the corresponding values of SNR_s in Fig. 7b, with the assumption that the quantization noise corresponds to an equivalent SNR_s). A coarse agreement between the simulated and the empirical values can be seen for a k of 1.25.

The improvement of the SF with the number of bits is asymptotic, as evident from Fig. 9, which shows the normalized SF area as a function of the bit resolution. A linear trend can be seen with the bit resolution up to 8 bits. The improvement with f_s is significant at higher bit resolutions than at lower bit resolutions, indicating the dependence of SNR_q on the sampling rate. The SF area at a f_s of 48 MHz is approximately 0.6 for a bit resolution of 8. Thus, the FOM for the SF at this f_s is approximately 60% of the theoretical SF.

DISCUSSION

The use of the measured value of the correlation coefficient to estimate SNR_e is robust and less sensitive to bias errors in TDE than a direct measure of SNR_e from the elastogram. Using ρ facilitates a direct comparison among theory, simulations and experiments, and could be used as a benchmark in comparing algorithms and apparatus (Srinivasan et al. 2002).

An asymptotic improvement of the FOM with sampling frequency is observed in the simulations. This improvement is primarily due to the use of linear interpolation to implement stretching. It is to be noted that, to implement stretching in a digital domain, interpolation of the A-lines at the modified sample locations (that are not integers) is performed. To confirm this hypothesis, simulations involving RF A-lines sampled at very high sampling rates (to mimic experiments, *i.e.,* an analog process) were performed and stretching the postcompression A-lines was done. This was followed by downsampling the A-lines and, subsequently, TDE of the downsampled A-lines. No sig-
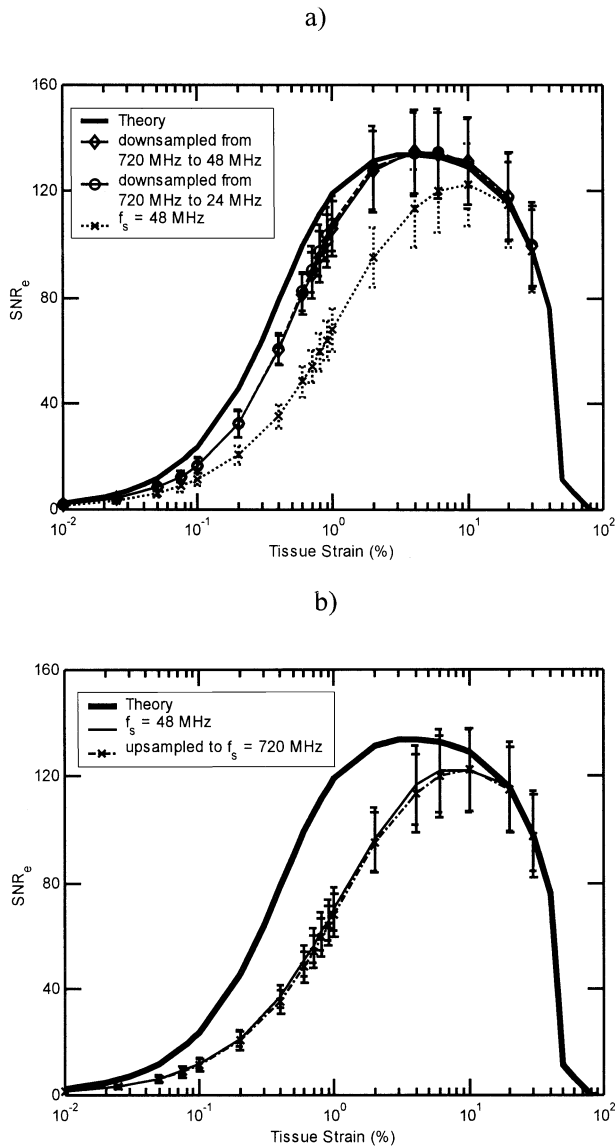
a)

b)

Fig. 10. SFs for (a) comparison of the SF at an f_s of 48 MHz with the SF generated by downsampling A-lines sampled at 720 MHz and downsampled to 48 MHz and 24 MHz; and (b) comparison of the SF at an f_s of 48 MHz with the SF generated by upsampling the A-lines to an f_s of 720 MHz. The SFs were obtained for a 5-MHz, 50% fractional bandwidth Gaussian PSF, and 3-mm window with a 50% overlap on a uniformly elastic phantom sample at a sampling frequency (f_s) of 96 MHz and an SNR_s of 40 dB. The error bars correspond to $\pm \, \sigma$ over 50 independent realizations.

nificant and/or consistent improvement of the SNR_e with the sampling frequency was observed (Fig. 10a). Such an interpolation was done to fit the theoretical model, eqns (A1) and (A3), which incorporates linear stretching. Using nonlinear interpolation schemes like cubic or spline interpolation improved the perfor-

mance at low sampling frequencies. This is because the interpolation is sensitive to the shape of the function (here, we have a cosine with a Rayleigh envelope). At high sampling frequencies, the results using cubic or spline interpolation were similar to those obtained using linear interpolation. Further, it is to be noted that a subsample interpolation of the cross-correlation peak is typically done in TDE.

Sampling the RF A-lines at a high frequency also improves the performance of the interpolation technique used in TDE (Céspedes et al. 1995a). However, in the absence of pure time delays (typical in elastography when stretching is incorporated), we expect the performance improvement due to interpolation of the cross-correlation function to be insignificant. To verify that, the tissue compression was avoided by stretching the point-spread function analytically, eqn (A3), and retaining the same tissue scatterer distribution for the pre- and postcompression signals. The results did not show significant improvement with the sampling frequency, unlike the situation where the tissue was compressed (Fig. 2a). Hence, in elastography, the role of sampling frequency is more significant in stretching the A-line than in the interpolation used for TDE. For the same reason, no significant improvement was observed when an unbiased interpolation, like the sinc interpolation instead of parabolic or cosine interpolation, was used for the TDE (Céspedes et al. 1995a). Note that, in the presence of residual time delays after stretching (which could occur due to incorrect stretching or nonhomogeneous phantoms), there still is an improvement of the TDE with increasing sampling frequencies due to a reduction of the bias and the random errors in the TDE (Céspedes et al. 1995).

Although the role of sampling frequency seems counterintuitive (i.e., the performance improves with the sampling frequency even although the Nyquist sampling theorem is assumed to be satisfied), it is to be noted that we use Gaussian spectra for the PSF. The use of Gaussian signal spectra implies that the noise introduced by aliasing is reduced by increasing the sampling frequency. Moreover, the shapes of the A-lines depend to a large extent on the shapes of the aliased A-lines and the interpolation of such aliased signals (to do stretching) improves with high sampling frequencies. The simulation model assumes the same power spectral shapes for both the additive noise and the signal A-lines. Hence, no improvement of the SF with upsampling the A-lines, after the addition of noise, is observed (Fig. 10b).

The improvement in the FOM with the number of quantization bits is predicted by an empirical model that assumes a very high sampling rate and a large number of bits. Although a coarse match between the

simulated results and the empirical model is found in some cases, the choice of some of the parameters in the model (k, SNR_s) to obtain such an agreement is not justified. However, an SNR improvement of approximately 6 dB per bit for sinusoidal signals is prevalent in the literature (Ziemer et al. 1983). We essentially obtained a similar improvement in SNR_s by assuming an effective number of bits that is a fraction of the actual number of bits (~ 0.8) (*i.e.,* an SNR_s improvement of approximately 4.8 dB per bit was observed).

Studies with respect to the other algorithmic and acoustic parameters, such as transducer band width, window length and window overlap, were performed and the results were consistent with previous observations (Varghese and Ophir 1997b).

CONCLUSION

An asymptotic improvement of the figure-of-merit with sampling frequency is observed in the simulations. Similarly, an asymptotic improvement of the figure-of-merit with the number of quantization bits was also observed. The noise introduced due to quantization was incorporated into an effective songographic SNR (SNR_s) and was then used to derate the SF. An improvement of approximately 4.8 dB per bit was found to agree well with the simulations. The area of the SF was used as a gross figure-of-merit of the SF and is expected to be useful in evaluating algorithms and apparatus. Such a figure-of-merit can be used to derate the SF with the sampling frequency. The analysis of the digitization aspects would help in the appropriate choice of the signal-processing parameters for a reliable elastographic system.

REFERENCES

Alam SK, Ophir J, Konofagou E. An adaptive strain estimator for elastography. IEEE Trans Ultrason Ferroelec Freq Control 1998; 45(2):461–472.

Bendat JS, Piersol AC. Random data: Analysis and measurement, 2nd ed. New York: John Wiley and Sons, 1986.

Bertrand M, Meunier M, Doucet M, Ferland G. Ultrasonic biomechanical strain gauge based on speckle tracking. Proc 1989 IEEE Ultrason Sympos 1989;2:859–864.

Carter GC. Coherence and time delay estimation. Proc IEEE 1987; 75(2):236–255.

Céspedes I. Elastography. Imaging of biological tissue elasticity. Ph.D. Dissertation. University of Houston, 1993.

Céspedes I, Ophir J. Reduction of image noise in elastography. Ultrason Imaging 1993;15:89–102.

Céspedes I, Huang Y, Ophir J, Spratt S. Methods for estimation of subsample time delays of digitized echo signals. Ultrason Imaging 1995a;17:142–171.

Céspedes I, Insana M, Ophir J. Theoretical bounds on strain estimation in elastography. IEEE Trans Ultrason Ferroelec Freq Control 1995b;42(5):969–972.

Céspedes I, Ophir J, Alam KS. The combined effect of signal decorrelation and random noise on the variance of time delay estimation. IEEE Trans Ultrason Ferroelec Freq Control 1997;44(1):220–225.

Chaturvedi P, Insana M, Hall TJ. 2-D companding for noise reduction in strain imaging. IEEE Trans Ultrason Ferroelec Freq Control 1998;45(1):179–191.

Kallel F, Varghese T, Ophir J, Bilgen M. The nonstationary strain filter in elastography: Part II. Lateral and elevational decorrelation. Ultrasound Med Biol 1997;23(9):1357–1369.

Knapp CH, Carter GC. The generalized correlation method for estimation of time delay. IEEE Trans Acoust Speech Sig Proc 1976;24: 320–327.

Meunier J, Bertrand M. Ultrasonic texture motion analysis: Theory and simulation. IEEE Trans Ultrason Ferroel Freq Control 1995a;14: 293–300.

Meunier J, Bertand M. Echographic image mean gray level changes with tissue dynamics: A system-based model study. IEEE Trans Biomed Eng 1995b;42(4):403–410.

O'Donnell M, Skovoroda AR, Shapo BM. Measurement of arterial wall motion using Fourier based speckle tracking algorithms. Proc 1991 IEEE Ultrason Sympos 1991;2:1101–1104.

Ophir J, Alam KS, Garra B, et al. Elastography. Ultrasonic estimation and imaging of the elastic properties of tissues. Engineering in Medicine, Part HJ. Proc Inst Mech Eng 1999;213:203–233.

Ophir J, Céspedes I, Garra B, et al. Elastography: Ultrasonic imaging of tissue strain and elastic modulus in vivo. Eur J Ultrasound 1996;49–70.

Ophir J, Céspedes I, Ponnekanti H, Yazdi Y, Li X. Elastography: A quantitative method for imaging the elasticity of biological tissues. Ultrason Imaging 1991;13:111–134.

Ophir J, Kallel F, Varghese T, et al. Elastography. A systems approach. Int J Imaging Syst Technol 1997;8:89–103.

Quazi AH. An overview on the time delay estimate in active and passive systems for target localization. IEEE Trans Acoust Speech Sig Proc 1981;29:527–533.

Srinivasan S, Kallel F, Ophir J. Estimating the elastographic signal-to-noise ratio using correlation coefficients. Ultrasound Med Biol 2002;28(3):359–368.

Trahey GE, Smith SW. Properties of acoustical speckle in the presence of phase aberration. Part I –First order statistics. Ultrason Imaging 1998;10:29–51.

Varghese T, Ophir J. Enhancement of echo-signal correlation in elastography using temporal stretching. IEEE Trans Ultrason Ferroelec Freq Control 1997a;44(1):173–180.

Varghese T, Ophir J. The nonstationary strain filter in elastography: Part I. Frequency dependent attenuation. Ultrasound Med Biol 1997b;23(9):1343–1356.

Varghese T, Ophir J. A theoretical framework for performance characterization of elastography: The strain filter. IEEE Trans Ultrason Ferroelec Freq Control 1997c;44(1):164–172.

Varghese T, Bilgen M, Ophir J. Phase aberration effects in elastography. Ultrasound Med Biol 2001;27(6):819–827.

Varghese T, Konofagou EE, Ophir J, Alam SK, Bilgen M. Direct strain estimation in elastography using spectral cross-correlation. Ultrasound Med Biol 2000;26(9):1525–1537.

Walker FH, Trahey EG. A fundamental limit on delay estimation using partially correlated speckle signals. IEEE Trans Ultrason Ferroelec Freq Control 1995;42:301–308.

Weinstein E, Weiss A. Fundamental limitations in passive time delay estimation—Part I: Narrow-band systems. IEEE Trans Acoust Speech Sig Proc 1984a;31(2):472–485.

Weinstein E, Weiss A. Fundamental limitations in passive time delay estimation—Part I: Wide-band systems. IEEE Trans Acoust Speech Sig Proc 1984b;31(5):1064–1078.

Zagzebski JA, Chen JF, Dong F, Wilson T. Intervening attenuation affects first-order statistical properties of ultrasound echo signals. IEEE Trans Ultrason Ferroel Freq Control 1999;46(1):35–40.

Ziemer RE, Tranter WH, Fannin DR. Signals and systems. New York: Macmillan, 1983.

APPENDIX A

THEORETICAL BOUNDS ON THE SF

Strain measurement in elastography involves estimating time delays between the pre- and postcompression A-lines followed by computing the gradients of these time delays. For a base signal $s_1(t)$, a delayed signal $s_1(t - D)$, and additive noise sources n_1, and n_2, the model (Varghese and Ophir 1997a) can be expressed as

$$r_1(t) = s_1(t) + n_1(t) = s(t)*p(t) + n_1(t)$$

$$r_2(t) = s\left(\frac{t}{a} - t_o\right)*p(t) + n_2(t), \qquad (A1)$$

where $s(t)$ is the scatterer function, $p(t)$ is the impulse response of the system (the point spread function, PSF), t_o is the time delay between the pre- and postcompression RF A-lines, and a is defined as $a = 1 - s$, where s is the applied strain. Here, s_1, n_1, and n_2 are real, stationary random processes. s_1 is uncorrelated with n_1 and n_2, which are both uncorrelated. The time-delay estimate (TDE) can be obtained through the correlation of r_1 and r_2 as

$$R_{r_1 r_2}(\tau) = E[r_1(t)r_2(t + \tau)] = \frac{1}{T - \tau}\int_\tau^T r_1(t)r_2(t + \tau)dt, \quad (A2)$$

where T represents the observation period.

The estimate of the time delay is the location of the peak of the cross-correlation function in the lag domain. For processing in a digital domain, interpolation around the peak sample is done to improve the accuracy of time-delay estimation.

Stretching the postcompression RF A-line ($r_2(t)$) by the factor a is done to undo the scaling effects of mechanical compression on the signal (Varghese and Ophir 1997b). The resulting A-line can be expressed as

$$r_3(t) = r_2(at) = s(t - t_o)*p(at) + n_2(at). \qquad (A3)$$

It can be seen that there is signal decorrelation due to strain in both $r_2(t)$ and $r_3(t)$. This is because the strain is a continuous function of t and it affects the scatterer function in $r_2(t)$ and the PSF in $r_3(t)$. Analytical expressions on the lowest bound on the variance, known as the Cramér–Rao lower bound (CRLB), has been obtained for TDE (Knapp and Carter 1976; Carter 1987; Quazi 1981) for correlated signals and pure time delays. The CRLB for partially correlated band-pass signals was obtained by Walker and Trahey (1995) and adapted to elastography by Céspedes et al. (1997) as

$$\sigma_{CRLB}^2 \cong \frac{3}{\pi^2 T f_o^3 (B^3 + 12B)}\left(\left(1 + \frac{1}{SNR_c}\right)^2 - 1\right), \qquad (A4)$$

where T is the segment length, f_o is the center frequency, B is the fractional bandwidth, and SNR_c is the combined SNR and is derived (Weinstein and Weiss 1984a, 1984b) as

$$SNR_c = \frac{SNR_\rho SNR_s}{1 + SNR_\rho + SNR_s}, \qquad (A5)$$

where SNR_s is the sonographic SNR and SNR_ρ is the correlation SNR (Céspedes and Ophir 1993) given by

$$SNR_\rho = \frac{\rho}{1 - \rho}, \qquad (A6)$$

and ρ is the correlation coefficient.

The threshold behavior of the variance has been adapted for elastography by Varghese and Ophir (1997b), in terms of the variation of the variance with the strain. The lower bound of the variance of the TDE (called as the Ziv–Zakai lower bound) (Weinstein and Weiss 1984a, 1984b) is given by

$$\sigma_{ZZLB}^2 = \begin{cases} \dfrac{(sT)^2}{6T\Delta T}, & BTSNR_c < \gamma \\ Threshold, & \gamma < BTSNR_c < \delta \\ 2\dfrac{\sigma_{BB}^2}{T\Delta T}, & \delta < BTSNR_c < \mu \\ Threshold, & \mu < BTSNR_c < \eta \\ 2\dfrac{\sigma_{CRLB}^2}{T\Delta T}, & \eta < BTSNR_c \end{cases} \qquad (A7)$$

The expressions for the thresholds γ, δ, μ and η are detailed in Varghese and Ophir (1997b) as

$$\eta = \frac{12}{\pi^2 T\Delta T}\left(\frac{f_0}{B}\right)^2\left[\varphi^{-1}\left(\frac{B^2}{24f_0^2}\right)\right]^2$$

$$\mu = \frac{5.52}{\pi^2 T\Delta T}\left(\frac{f_0}{B}\right)^2$$

$$\delta = \zeta/T\Delta T$$

$$\gamma \approx 0.92/T\Delta T \qquad (A8)$$

where

$$\varphi(y) = \frac{1}{\sqrt{2\pi}}\int_y^\infty e^{-\mu^2/2}d\mu, \text{ and } (\zeta/2)\varphi(\sqrt{\zeta/2}) = (12\pi/BsT)^2 \qquad (A9)$$

and the Barankin bound is given by

$$\sigma_{BB}^2 = 12\left(\frac{f_o}{B}\right)^2\sigma_{CRLB}^2. \qquad (A10)$$

The SD of the strain σ_s is related to the SD of the TDE σ_t by

$$\sigma_s^2 \geq \frac{2\sigma_t^2}{T\Delta T}, \qquad (A11)$$

where ΔT is the separation between adjacent time segments (Céspedes et al. 1995b). The expression for the SNR_e is given by

$$SNR_e = \frac{\mu_m}{\sigma_m}, \qquad (A12)$$

where μ_m is the mean value of the measured strain and σ_m is the SD of the measured strain. The upper bound of the SNR_e is obtained by substituting s instead of μ_m, σ_s instead of σ_m, and the σ_{ZZLB} instead of σ_t in eqn (A12).

APPENDIX B

USING THE CORRELATION COEFFICIENT TO COMPUTE SNR_E

Biased interpolation for estimating time delays tends to produce smooth strain estimates and results in image artefacts such as image periodicities, commonly known as "zebras and worms"(Ophir et al. 1999; Céspedes 1993). This could result in higher elastographic SNR (SNR_e) values that are not representative of the expected values and could result in loss of image contrast. As an illustration, consider a TDE estimation where no subsample interpolation is performed (*i.e.,* the sample corresponding to the correlation peak is taken as the true TDE); this corresponds to a highly biased interpolator. For such a case, the TDE on a uniformly elastic phantom would most likely fall at the same sample location (the first sample if there is no shift between the A-lines) for each segment. Hence, the strain estimates for all the segments would be identical to each other, resulting in an infinite SNR_e despite the presence of additive noise or imperfect stretching (Varghese and Ophir 1997a; Céspedes 1993). Thus, biased interpolation could result in a high SNR_e that does not represent the signal decorrelation between the pre- and postcompression RF A-lines. Additionally, postprocessing the elastogram (such as low-pass filtering the elastogram) could improve the SNR_e without changing the correlation coefficient (ρ) between the pre- and the postcompression A-lines, implying a lack of consistency in computing SNR_e directly from the elastogram.

To avoid these image-related problems, we use the estimated value of ρ to compute the SNR_e indirectly as follows. The estimated value of ρ is used in eqn (4) to compute the SNR_ρ. This computed value of SNR_ρ is used in eqn (3) to compute the SNR_c, which, in turn, is used in eqn (A7) to estimate the σ_{ZZLB}. Equation (2) is then used to compute the lower bound on σ_s (the lower bound is obtained when $\sigma_t = \sigma_{ZZLB}$) and eqn (1) uses σ_s to compute the SNR_e. This results in SNR_e values that are bounded by the SF theory and also facilitates a direct comparison of simulations and experiments with the theory. More details on the use of ρ to compute the SNR_e can be found in Srinivasan et al. (2002).

APPENDIX C

SENSITIVITY ANALYSIS WITH RESPECT TO THE CORRELATION COEFFICIENT P

The CRLB for TDE in elastography, eqn (A4) is given by

$$\sigma_{CRLB}^2 \cong \frac{3}{\pi^2 T f_o^3 (B^3 + 12B)} \left(1 + \frac{1}{SNR_c}\right)^2 - 1, \qquad (C1)$$

where T is the segment length, f_o is the center frequency, B is the fractional band width, and SNR_c is the combined SNR, defined as

$$SNR_c = \frac{SNR_\rho SNR_s}{1 + SNR_\rho + SNR_s}. \qquad (C2)$$

SNR_s is the sonographic SNR, and SNR_ρ is the correlation SNR, defined as

$$SNR_\rho = \frac{\rho}{1 - \rho}. \qquad (C3)$$

The upper bound of the SNR_e is given by

$$SNR_e = \frac{s}{\sigma_s}, \qquad (C4)$$

where s is the applied strain and σ_s is the lower bound of the variance of the measured strain, given in Céspedes aln. (1995b) as

$$\sigma_{s2} = \frac{2\sigma_{CRLB}^2}{T \Delta T}. \qquad (C5)$$

Therefore, from eqns (C5), (C4) and (C1), we have

$$SNR_e = \frac{s \sqrt{\dfrac{T \Delta T}{2}} \sqrt{\dfrac{\pi^2 T f_o^3 (B^3 + 12B)}{3}}}{\sqrt{\left(1 + \dfrac{1}{SNR_c}\right)^2 - 1}} \qquad (C6)$$

or

$$SNR_e = \frac{k}{\sqrt{\left(1 + \dfrac{1}{SNR_c}\right)^2 - 1}}, \qquad (C7)$$

where k is the numerator in eqn (C6). Equation (C2) can be approximated as

$$SNR_c \cong \frac{SNR_\rho SNR_s}{SNR_\rho + SNR_s}. \qquad (C8)$$

Using eqn (C8) in (C7), we obtain

$$SNR_e = \frac{k}{\sqrt{\left(1 + \dfrac{1}{SNR_s} + \dfrac{1}{SNR_\rho}\right)^2 - 1}}. \qquad (C9)$$

Simplifying eqn (C9) and using eqn (C3), we obtain

$$SNR_e = \frac{k}{\sqrt{\left(k_1 + \dfrac{1 - \rho}{\rho}\right)^2 - 1}}, \qquad (C10)$$

where

$$k_1 = 1 + \frac{1}{SNR_s}. \qquad (C11)$$

Now

$$\frac{dSNR_e}{d\rho} = \frac{1}{2\rho^2} k \left(\left(k_1 + \frac{1 - \rho}{\rho}\right)^2 - 1\right)^{-3/2} \left(k_1 + \frac{1 - \rho}{\rho}\right). \qquad (C12)$$

that is

$$\frac{dSNR_e}{d\rho} = \frac{1}{2\rho^2} k \left(\left(k_1 + \frac{1 - \rho}{\rho}\right)^2 - 1\right)^{-3/2} \left(k_1 + \frac{1 - \rho}{\rho}\right). \qquad (C13)$$

This is a nonlinear function of ρ. In this expression, k is assumed to be a constant. However,

$$k = s \sqrt{\frac{T \Delta T}{2}} \sqrt{\frac{\pi^2 T f_o^3 (B^3 + 12B)}{3}} \qquad (C14)$$

and ρ as a function of strain s is given in Varghese and Ophir (1997a) as

$$\rho = \left(\frac{\sqrt{2(1-s)}}{(1 + e^{-(\sigma k_o)^2}) \sqrt{(1-s)^2 + 1}} \right)$$

$$\times \left(e^{-\left(\frac{(\sigma k_o)^2}{2} \frac{s^2}{((1-s)^2+1)} \right)} + e^{-\left(\frac{(\sigma k_o)^2}{2} \frac{(2-s)^2}{((1-s)^2+1)} \right)} \right). \qquad (C15)$$

Equations (C14) and (C15) can be incorporated into eqn (C10) and the derivative can then be obtained. However, obtaining s as a function of ρ is rather involved and, hence, obtaining a closed form solution for the sensitivity of SNR_e with respect to ρ is complicated. A simpler method would be to effect a change in ρ and obtain SNR_e numerically. Figure C1 shows the change in the SF for a 0.2% standard deviation in ρ. A comparison of the standard deviation in SNR_e for the theoretical and the simulated results (corresponding to the 192 MHz case in Fig. 3) indicates the strain dependence. For the theory, σ_ρ was held constant and σ_ρ varies with the strain in the simulations. If we accommodate the change in σ_ρ, using eqn (C15), then we can have a quantitative comparison of the simulation σ_{SNR} with those allowed by the theory.
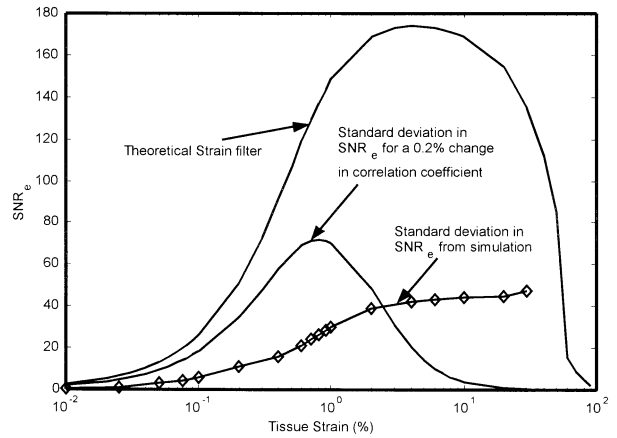

Fig. C1. Theoretical SF and the SD in the SF corresponding to a σ_ρ of 0.2% for a 5-MHz, 50% band width Gaussian PSF and 3-mm window with a 50% overlap on a uniformly elastic phantom at an SNR_s of 40 dB. ($\diamond$) the simulation results of Fig. 5b.